GEOPHYSICS, VOL. 82, NO. 3 (MAY-JUNE 2017); P. T111–T120, 10 FIGS.
10.1190/GEO2016-0212.1

A simple finite-difference scheme for handling topography with the second-order wave equation

W. A. Mulder[1]

ABSTRACT

The presence of topography poses a challenge for seismic modeling with finite-difference codes. The representation of topography by means of an air layer or vacuum often leads to a substantial loss of numerical accuracy. A suitable modification of the finite-difference weights near the free surface can decrease that error. An existing approach requires extrapolation of interior solution values to the exterior while using the boundary condition at the free surface. However, schemes of this type occasionally become unstable and may be impossible to implement with highly irregular topography. One-dimensional extrapolation along coordinate lines results in a simple and efficient scheme. The stability of the 1D scheme is improved by ignoring the interior point nearest to the boundary during extrapolation in case its distance to the boundary is less than half a grid spacing. The generalization of the 1D scheme to more than one dimension requires a modification if the boundary intersects the finite-difference stencil on both sides of the central evaluation point and if there are not enough interior points to build the finite-difference stencil. Examples for the 2D constant-density acoustic case with a fourth-order finite-difference scheme demonstrate the method's capability. Because the 1D assumption is not valid in two dimensions if the boundary does not follow grid lines, the formal numerical accuracy is not always obtained, but the method can handle highly irregular topography.

INTRODUCTION

The incorporation of topography, the ultimate contrast, in seismic modeling codes poses a challenge for finite-difference codes. There are several ways to deal with the problem. The simplest is the inclusion of a density contrast to mimic an air layer, at the expense of numerical accuracy. For elastic wave propagation, Bartel et al. (2000) find that some smoothing of the extreme density contrast is required for numerical stability. Boore (1972), Robertsson (1996), Mittet (2002), Bohlen and Saenger (2006), and Zeng et al. (2012) consider variants of the vacuum approach. Unfortunately, the loss of accuracy can become significant: Numerical experiments with a higher order finite-difference scheme for the acoustic wave equation indicate that the numerical error increases to only the first order in space (Zhebel et al., 2014) in case of a smoothed density contrast. The cause is the same as for large subsurface contrasts: The solution is not differentiable across sharp interfaces, leading to a second-order spatial error, and if the subsurface model is just sampled, the position of the interface is uncertain within a grid spacing, leading to a first-order error. Averaging instead of sampling can reduce the latter but still leaves the second-order error.

If the topography is gradual and smooth, locally orthogonal boundary-fitted coordinates will work (e.g., Tessmer and Kosloff, 1994; Hestholm and Ruud, 1998, 2002; De la Puente et al., 2014). The more general case requires a finite-element approach (e.g., Komatitsch and Vilotte, 1998; Etienne et al., 2010; Zhebel et al., 2011) or a mimetic finite-difference method (for a review, see Lipnikov et al., 2014). Both tend to increase the computing cost. An alternative is the modification of the finite-difference operator near the boundary.

Local modification of the finite-difference stencil near the free surface may improve accuracy without a substantial cost increase. Shortley and Weller (1938) present one of the earliest schemes of a modified numerical scheme for a boundary not coinciding with the grid, solving Laplace's equation. Several authors follow that approach for the wave equation, for instance, Strand (1994), Carpenter et al. (1999), Piraux and Lombard (2001), Mattsson and Nordström (2006), Lombard et al. (2008), Mattsson et al. (2009), Fornberg (2010), Seo and Mittal (2011), AlMuhaidib et al. (2011), Zhang et al. (2013), Gao et al. (2015), and Hu (2016).

Zhang et al. (2013) consider simple 1D extrapolation and zero pressure on the free surface for the acoustic wave equation. They

Manuscript received by the Editor 22 April 2016; revised manuscript received 2 December 2016; published online 10 April 2017.
[1]Shell Global Solutions International B.V., Rijswijk and Delft University of Technology, Faculty of Civil Engineering and Geosciences, Department of Geoscience and Engineering, Delft, The Netherlands.

ignore the additional boundary condition that its second and higher order even time derivatives should also remain at zero on the boundary. Lombard et al. (2008) exploit the fact that the latter can be translated into spatial derivatives by means of the partial differential equation. They propose a scheme that extrapolates interior values to fictitious exterior values, using these boundary conditions together with a polynomial fit through a number of interior points to obtain the desired numerical accuracy. To avoid stability problems, they choose more interior points than are strictly needed, resulting in an overdetermined system of equations. The least-squares solution of this system provides the extrapolating polynomial. They report that their scheme can still be unstable in some cases.

Here, I consider a simpler 1D scheme for the second-order formulation of the constant-density acoustic wave equation, based on this extrapolation idea. Admittedly, the simplification of the elastic system of wave equations to constant-density acoustics is of limited value for modeling, migration, and inversion of land seismic data, but it can still be useful for some applications.

To avoid a reduction in performance, the proposed method should have the same time-stepping stability limit (Courant et al., 1928) as the interior finite-difference scheme. Also, the extrapolation scheme only acts in the construction of a modified 1D finite-difference operator, independently for each coordinate direction. This avoids ambiguities and the associated instabilities in special circumstances that arise in two dimensions and three dimensions. Although the scheme does not preserve the formal accuracy of the interior finite-difference discretization, it remains stable in extreme cases. After a description of the method, a set of 2D numerical experiments will demonstrate the capabilities of the method.

METHOD

1D case

Before examining the 2D case, we can learn a few things in one dimension. Consider the 1D second-order constant-density acoustic wave equation:

$$\frac{1}{c^2}\frac{\partial^2 u}{\partial t^2}-\frac{\partial^2 u}{\partial x^2}=f, \tag{1}$$

with pressure $u(t,x)$, sound speed $c(x)$, and optional source term $f(t,x)$. The solution is represented on a grid with points $x_i=x_0+i\Delta x$, where $i=0,1,\ldots,N_x-1$. The standard spatial discretization of even order M is

$$\left.\frac{\partial^2 u}{\partial x^2}\right|_{x_i}\simeq\frac{(\mathbf{D}_{xx}\mathbf{u})_i}{(\Delta x)^2},$$

$$-(\mathbf{D}_{xx}\mathbf{u})_i=w_0u_i+\sum_{k=1}^{M/2}w_k(u_{i+k}+u_{i-k}), \tag{2}$$

where

$$w_0=\sum_{j=1}^{M/2}\frac{2}{j^2},\quad w_k=(-1)^k\sum_{j=k}^{M/2}\frac{2}{j^2}\frac{(j!)^2}{(j-k)!(j+k)!}, \tag{3}$$

for $k=1,\ldots,M/2$ (Fornberg, 1987, a.o.). A second-order time stepping scheme is

$$u_i^{n+1}-2u_i^n+u_i^{n-1}=\left(\frac{c_i\Delta t}{\Delta x}\right)^2(\mathbf{D}_{xx}\mathbf{u}^n)_i+\Delta t^2 f_i^n, \tag{4}$$

with the time sampled at $t^n=t^0+n\Delta t$. The Cauchy-Kowalewski or Lax-Wendroff procedure (Lax and Wendroff, 1960) provides higher order time stepping by substituting higher time derivatives with spatial derivatives using the partial differential equation. Other names for this method are Dablain's (1986) scheme or the modified-equation approach (Shubin and Bell, 1987)

Let the boundary at the right side of the domain be located at the point $x_b=x_{N_x-1}+\xi\Delta x$, with $\xi\in(0,1]$. Following Piraux and Lombard (2001) and Lombard et al. (2008), we should have $\partial^{2k}u/\partial t^{2k}(t,x_b)=0$ on the boundary for $k=0,1,\ldots$. If $c(x)$ is constant near the boundary, this translates into zero even spatial derivatives $\partial^{2k}u/\partial x^{2k}(t,x_b)=0$. We can construct an extrapolating polynomial of even degree M of the form $u(x)=\sum_{k=0}^{M}b_k(x-x_b)^k$. The $1+M/2$ boundary conditions imply $b_k=0$ for $k=0,2,\ldots,M$ and the remaining coefficients for $k=1,3,\ldots,M-1$ follow from fitting solution values at an additional $M/2$ interior grid points. Figure 1 sketches an example for an eighth-order discretization ($M=8$). Note that antisymmetric mirroring of the solution with respect to the boundary point followed by Lagrange interpolation provides the same results.

In the fourth-order case with $M=4$, the extrapolation formula becomes

$$\begin{pmatrix}u_{N_x}\\u_{N_x+1}\end{pmatrix}=\mathbf{E}^{\mathrm{I}}\begin{pmatrix}u_{N_x-2}\\u_{N_x-1}\end{pmatrix},$$

$$\mathbf{E}^{\mathrm{I}}=\begin{pmatrix}-\frac{(1-\xi)(1-2\xi)}{(1+\xi)(1+2\xi)} & -\frac{4(1-\xi)}{1+2\xi}\\ -\frac{4(2-\xi)(1-\xi)}{(1+\xi)(1+2\xi)} & \frac{3(2-\xi)(1-2\xi)}{\xi(1+2\xi)}\end{pmatrix}. \tag{5}$$

Unfortunately, this scheme, labeled I, becomes unstable when the boundary sits close to the last interior grid point, when $\xi\downarrow 0$. In the fourth-order case, the element $E^{\mathrm{I}}_{2,2}$ that has ξ in the denominator will then grow without bounds as ξ approaches zero. The instability can be suppressed by decreasing the time step, as shown in Appendix A.

Choosing interior points that lie further away can improve the stability, as illustrated in Figure 1b. Scheme II switches from the stencil in Figure 1a to that in Figure 1b when ξ becomes too small, for instance, for $\xi_0=1/2$, meaning less than half a grid spacing. The mirroring and interpolation procedure ignores the grid point close to the boundary. The extrapolation scheme for a fourth-order scheme with $M=4$ becomes

$$\begin{pmatrix}u_{N_x}\\u_{N_x+1}\end{pmatrix}=\mathbf{E}^{\mathrm{II}}\begin{pmatrix}u_{N_x-3}\\u_{N_x-2}\end{pmatrix},$$

$$\mathbf{E}^{\mathrm{II}}=\begin{pmatrix}\frac{4\xi(1-\xi)}{(2+\xi)(3+2\xi)} & -\frac{3(1-\xi)(1+2\xi)}{(1+\xi)(3+2\xi)}\\ -\frac{3(2-\xi)(1-2\xi)}{(2+\xi)(3+2\xi)} & -\frac{8\xi(2-\xi)}{(1+\xi)(3+2\xi)}\end{pmatrix}. \tag{6}$$

Appendix A demonstrates that the time step does not have to be decreased when using scheme II.

Extrapolation gets messy in two dimensions with, for instance, the model of Figure 7a. A more manageable approach is the modification of the interior stencil. We can reformulate the earlier

extrapolation scheme as a modified interior finite-difference scheme for points near the boundary by application of the standard finite-difference weights in equation 3 to the combined set of interior and extrapolated values.

As an example, there are four cases for order $M = 4$, apart from the interior finite-difference stencil for the second derivative given by

$$\mathbf{w} = \left(\frac{1}{12}, -\frac{4}{3}, \frac{5}{2}, -\frac{4}{3}, \frac{1}{12}\right). \tag{7}$$

If the finite-difference stencil needs one exterior value to the right and $(1/2) \le \xi \le 1$, the modified finite-difference stencil becomes

$$\bar{\mathbf{w}} = \left(\frac{1}{12}, -\frac{4}{3}, \frac{29 + \xi(93 + 58\xi)}{12(1 + \xi)(1 + 2\xi)}, -\frac{5 + 7\xi}{3(1 + 2\xi)}, 0\right), \tag{8}$$

whereas for $0 < \xi < (1/2)$

$$\bar{\mathbf{w}} = \left(\frac{1}{12}, -\frac{8 + 3\xi(3 + \xi)}{(2 + \xi)(3 + 2\xi)}, \frac{29 + \xi(49 + 22\xi)}{4(1 + \xi)(3 + 2\xi)}, -\frac{4}{3}, 0\right). \tag{9}$$

If the stencil needs two exterior points and $(1/2) \le \xi \le 1$, the stencil's coefficients are

$$\bar{\mathbf{w}} = \left(\frac{1}{12}, -\frac{2 + \xi(21 + \xi)}{3(1 + \xi)(1 + 2\xi)}, \frac{6 + \xi(79 + 2\xi)}{12\xi(1 + 2\xi)}, 0, 0\right), \tag{10}$$

and for $0 < \xi < (1/2)$

$$\bar{\mathbf{w}} = \left(\frac{\xi(10\xi - 7)}{2(2 + \xi)(3 + 2\xi)}, -\frac{2\xi(2 + 5\xi)}{(1 + \xi)(3 + 2\xi)}, \frac{5}{2}, 0, 0\right). \tag{11}$$

Note that with $\xi < (1/2)$, the standard coefficient appears for the point closest to the boundary because the extrapolation operator ignores it and instead takes the two points further inward.

Similar expressions follow for higher orders. A computer algebra package will provide expressions for all cases as a function of ξ. Alternatively, it can be more convenient to determine the extrapolation operator $\mathbf{E}$ numerically where needed, mix it with the identity operator for the interior part into a symmetric operator of size $(M + 1) \times (M + 1)$, and then left multiply with the interior finite-difference stencil, $\mathbf{w}$, to obtain modified stencil weights, $\bar{\mathbf{w}} = \mathbf{wE}$. The latter are stored for repeated use during time stepping.

A 1D numerical example is a traveling pulse of the form $u(x, t) = [\max(0, 4\zeta(1 - \zeta))]^{12}$, with $\zeta = 4(x - ct) - 1$ and $c = 1$ on the interval $[0, 1 + \xi\Delta x]$ and with zero Dirichlet boundary conditions. It runs for a maximum time of $T = 2(1 + \xi\Delta x)$ when the pulse has returned to its original position after two reflections. Figure 2 shows the maximum error obtained on a grid with 201 points and a grid spacing of $\Delta x = 1/200$ as a function of $\xi \in (0, 1]$. Scheme I becomes unstable if the boundary sits too close to a grid point, whereas scheme II remains stable. Schemes of order $M = 4$ and 6 lead to similar results, also with larger values of ξ_0 up to or even beyond 1, i.e., one grid spacing.

2D case

The numerical examples presented later on only involve the fourth-order spatial discretization. Therefore, the description of the method will focus on this scheme with $M = 4$. The topography is assumed to be given as a cubic spline curve or piecewise cubic Hermite interpolating polynomial. Coding becomes simpler if the boundary representation is a function $z_b(x)$, singly valued by definition, which excludes overhangs and caves.

The representation of the 2D Laplace operator by the sum of two 1D discrete second derivatives along grid lines makes the application of the 1D scheme presented above straightforward, but there some pitfalls. Figure 3 sketches an example of a finite-difference grid and a free-surface boundary. The scheme only uses the values at the interior points, marked by crosses. The evaluation of the finite-difference stencil in a given point requires $M/2$ points in each direction, left, right, above, and below that central point, with $M/2 = 2$ in the present discussion. Note that "above" refers to decreasing z, in the direction of the zenith.

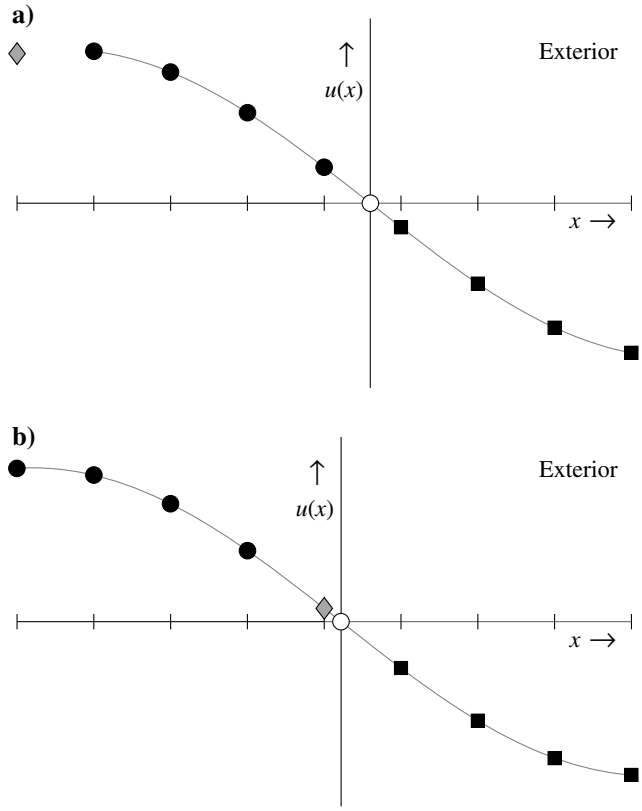

Figure 1. Extrapolation for a scheme of order $M = 8$ if the boundary point (open circle) does not lie too close to the last grid point. The solution at four interior grid points is marked by black dots. Together with four boundary conditions, the even spatial derivatives from zero to six being zero, this defines a unique polynomial of degree 7 that provides the four points denoted by black squares. These can be used for evaluation of the discrete spatial operator in the interior, which requires nine points, four on each side of the point where the discrete second derivative is evaluated. The extrapolation does not involve the point marked by a diamond. Scheme II, shown in panel (b), ignores the interior point nearest to the boundary if its distance to the boundary is smaller than half a grid spacing. Otherwise, Scheme I in panel (a) is adopted.

In the vertical direction, the stencil can intersect the boundary at most once because of the assumption that the boundary be a function of x. Then, the above 1D scheme applies, but with the finite-difference weights in reversed order because we have now assumed that the free-surface boundary occurs toward the left end of the grid line instead of the right.

If the boundary intersects a horizontal grid line once, again the 1D scheme applies. If the intersection occurs toward the right of the central point where the second spatial derivative is evaluated, one of the sets of the finite-difference weights in equations 8–11 applies. If the intersection occurs toward the left, one of those needs to be reversed.

The scheme becomes more complicated if the boundary intersects a horizontal grid line on both sides of the central point, where the second spatial derivative has to be evaluated. This happens for the two horizontal grid lines at the top of Figure 3. To distinguish between several cases, assume that the horizontal second derivative has to be evaluated at x_c and define $\eta = (x - x_c)/\Delta x$. The nearest intersection points with the boundary are $\eta_L < 0$ on the left and $\eta_R > 0$ on the right.

The standard interior difference weights in equation 7, approximating $-D_{xx}$, are valid if $\eta_L \le -2$ and $\eta_R \ge 2$. If $-\eta_L = 2$, the first weight may be set to zero and if $\eta_R = 2$, the last, although this should be superfluous because those cases correspond to a grid point precisely on the boundary where the pressure is zero. If $\eta_L < -2$ and $\eta_R < 2$, the 1D scheme applies, with one of the expression in equations 8–11. More precisely, if $\eta_R < ½$, equation 11 with $\xi = \eta_R$ applies, otherwise if $\eta_R < 1$, equation 10 with $\xi = \eta_R$, otherwise if $\eta_R < (3/2)$, equation 9 with $\xi = \eta_R - 1$, and otherwise, equation 8 with $\xi = \eta_R - 1$. In the case of $\eta_L > -2$ and $\eta_R > 2$, the same approach applies with the pair (η_L, η_R) changed to $(-\eta_R, -\eta_L)$ and the resulting weights are taken in reverse order.

That leaves the case in which the boundary intersects the stencil on both sides of the central point, with $-2 < \eta_L$ and $\eta_R < 2$. One way to implement the scheme is to start with the extrapolation operator $\mathbf{E}$, initialized as the identity matrix, $\mathbf{I}_{5\times5}$. After modification of $\mathbf{E}$, the modified finite-difference weights become $\bar{\mathbf{w}} = \mathbf{w}\mathbf{E}$, where $\mathbf{w}$ refers to the standard weights of equation 7 represented as a row vector.

First, we set $E_{j,j} = 0$ for those $j = 1, 2, \ldots, 5$ that obey $j - 3 \le \eta_L$ or $j - 3 \ge \eta_R$. Alternatively, $\mathbf{E}$ can be initialized with zeros followed by $E_{j,j} = 1$ for $\eta_L < j - 3 < \eta_R$. Next, consider the right side of the stencil, intersected at $\eta_R < 2$. If $\eta_R = 0$, we are on the boundary and can set all entries of $\mathbf{E}$ to zero. If not, let $k_R = \text{floor}(\eta_R)$, which is either 0 or 1, and $\xi = \eta_R - k_R \in [0, 1)$. Select $\mathbf{E}^{\text{R}} = \mathbf{E}^{\text{II}}$, given in equation 6, if $0 < \xi < (1/2)$ and $\mathbf{E}^{\text{R}} = \mathbf{E}^{\text{I}}$ in equation 5 otherwise. Next, we should copy elements of the small matrix $\mathbf{E}^{\text{R}}$ to a subset of the 5×5 matrix $\mathbf{E}$. The two target columns of $\mathbf{E}$ have indices j_R and $j_R + 1$, with $j_R = k_R + 1$ if $\xi < (1/2)$ and $j_R = k_R + 2$ for $(1/2) \le \xi < 1$. There are either one or two rows for $\mathbf{E}$, starting at $i_R = 4 + k_R$ up till row five. The assignment from the smaller to the larger matrix is

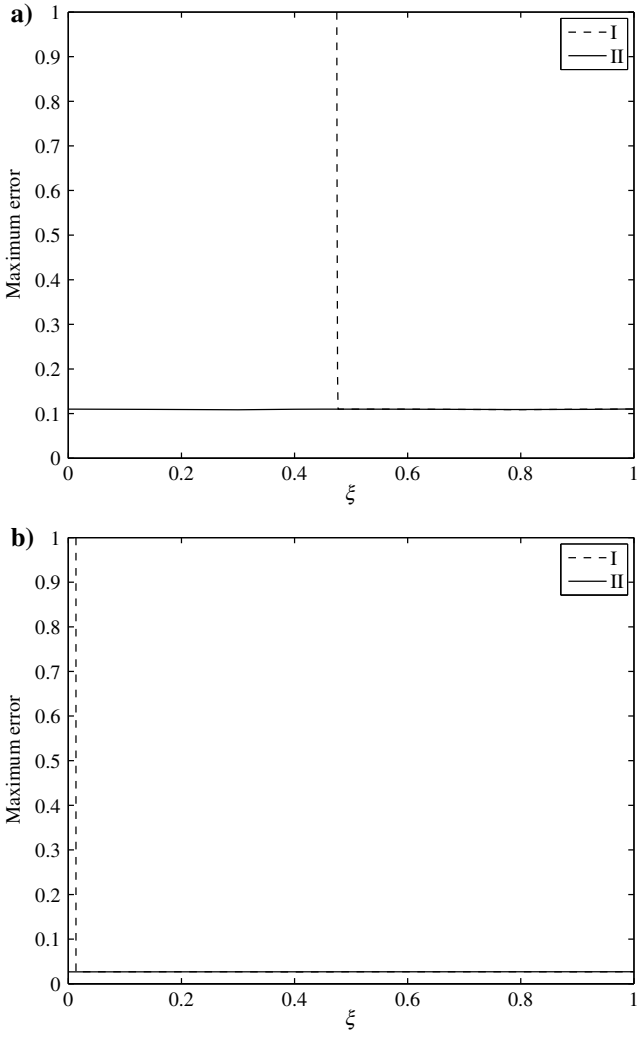

Figure 2. Maximum error for a test problem as a function of ξ with scheme I or II for order eight in space. The time step is taken at 100% of the stability limit for panel (a) and at 50% for (b). Extrapolation with scheme I (dashed line) causes an instability for $\xi \lesssim 0.48$ in panel (a) and $\xi \lesssim 0.0135$ in (b). Scheme II (drawn line) remains stable, with a maximum error that is almost independent of ξ.

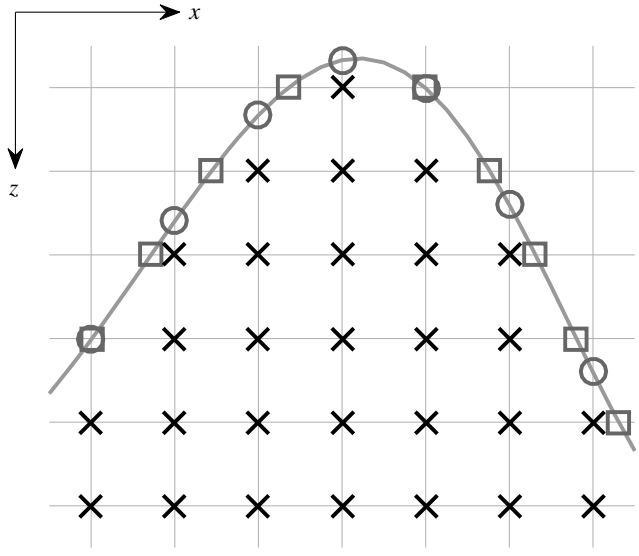

Figure 3. Example of a finite-difference grid. The crosses mark the interior grid points. The grid lines intersect the boundary at the top at the circles, in the vertical direction, or squares in the horizontal direction. The 1D extrapolation along grid lines produces different values in the exterior for horizontal and for vertical extrapolation.

$$E_{i,j} = E^{\mathrm{R}}_{i-i_R+1,j-j_R+1}, \quad i = i_R, \ldots, 5, \quad j = j_R, j_R+1. \tag{12}$$

Note that this approach fails if $j_R - 3 \le \eta_L$, which happens if there are insufficient interior points for one of the extrapolation formulas. If $j_R - 3 \le \eta_L$ but $j_R - 2 \ge \eta_L + (1/2)$, meaning the first point needed for interpolation has ended up in the exterior but the second point lies in the interior at a distance of at least half a grid spacing away from the left boundary position. The extrapolation then follows from the single interior point at index $j_R + 1$ and the zero boundary value at η_L:

$$E^{\mathrm{R}}_{i-i_R+1,1} = 0, \quad E^{\mathrm{R}}_{i-i_R+1,2} = \frac{\psi(i-3;\eta_L,\eta_R)}{\psi(j_R-2;\eta_L,\eta_R)}, \quad i = i_R, \ldots, 5, \tag{13}$$

where

$$\psi(\eta;\eta_L,\eta_R) = (\eta-\eta_L)(\eta-\eta_R)[(\eta_R-\eta_L)-(\eta-\eta_R)]. \tag{14}$$

Note that $j_R - 2$ refers to the relative position of the single interior point and is either -1 or 0.

For the left side of the stencil, if intersected at $-2 < \eta_L$, the same approach follows on the basis of symmetry. We just have to replace the pair (η_L, η_R) with $(-\eta_R, -\eta_L)$ and change the assignment in equation 12 to $E_{6-i,6-j} = E^{\mathrm{R}}_{i-i_R+1,j-j_R+1}$.

This leaves the case where the right-most point, indexed by $j_R + 1$, of the two points included in the extrapolation, lies to the left of $\eta_L + (1/2)$, that is, if $j_R - 2 < \eta_L + (1/2)$. Then, a parabolic fit to the central point and the two nearby zero-boundary values results in finite-difference weights $(0, 0, \bar{w}, 0, 0)$ with $\bar{w} = 2/(-\eta_L\eta_R)$. To avoid instabilities due to too small η_L or η_R, they are set to at least a 1/2: $\bar{w} = 2/[\max([1/2], -\eta_L)\max([1/2], \eta_R)]$. Note that this situation occurs when $-(3/2) < \eta_L < \eta_R < (1/2)$ or when $-(1/2) < \eta_L < \eta_R < (3/2)$. As a result, and also because the 2D boundary conditions are only approximately honored, we will lose the formal fourth-order accuracy.

As an aside, with the definition of ψ in equation 14, the operators in equations 5 and 6 become

$$\mathbf{E}^{\mathrm{I}} = \begin{pmatrix} \frac{\psi(\ 1;0,\xi)}{\psi(-1;0,\xi)} & \frac{\psi(1;-1,\xi)}{\psi(0;-1,\xi)} \\ \frac{\psi(\ 2;0,\xi)}{\psi(-1;0,\xi)} & \frac{\psi(2;-1,\xi)}{\psi(0;-1,\xi)} \end{pmatrix}, \quad \mathbf{E}^{\mathrm{II}} = \begin{pmatrix} \frac{\psi(\ 1;-1,\xi)}{\psi(-2;-1,\xi)} & \frac{\psi(\ 1;-2,\xi)}{\psi(-1;-2,\xi)} \\ \frac{\psi(\ 2;-1,\xi)}{\psi(-2;-1,\xi)} & \frac{\psi(\ 2;-2,\xi)}{\psi(-1;-2,\xi)} \end{pmatrix}. \tag{15}$$

Note, however, that this form does not reveal the occasional cancellation of common factors in the numerator and denominator.

For a fourth-order scheme, the solution should satisfy $\partial^m u(t, x(s), z(s))/\partial s^m = 0$ for $m = 0, \ldots, 3$ on the boundary parameterized by s, and also $0 = \partial^2 u/\partial t^2 = c^2 \Delta u$. The 1D scheme implies the assumption that the stencil intersects the boundary perpendicularly, which is not correct and will result in a numerical error. Lombard et al. (2008) avoid this simplification and, therefore, their scheme maintains the formal accuracy, but I could not get it to work with the very rough topography shown in Figure 7a.

RESULTS

Of the six test problems, the first three have an exact solution and offer insight in the error behavior of the method. The first has a point source in a constant-velocity model with a dipped surface at various angles. For the second and third problems, conformal mapping provided closed-form expressions for the velocity models and solutions. One has mild topography, the other a sharp corner and steep dips. The fourth problem, designed to test the method to its limits, has a highly irregular surface. The fifth and sixth problems mimic real-life problems. Points extracted from digital elevation maps served as input for the 2D topography, on top of a synthetic subsurface model.

The first example has a constant velocity of 2 km/s. The surface crosses the origin and has dip angles ϕ between 0° and 45° at a 5° increment. A source is placed at $x_s = 0$ m and $z_s = 60/\cos\phi$ m, and it is numerically represented by a tapered sinc function (Hicks,

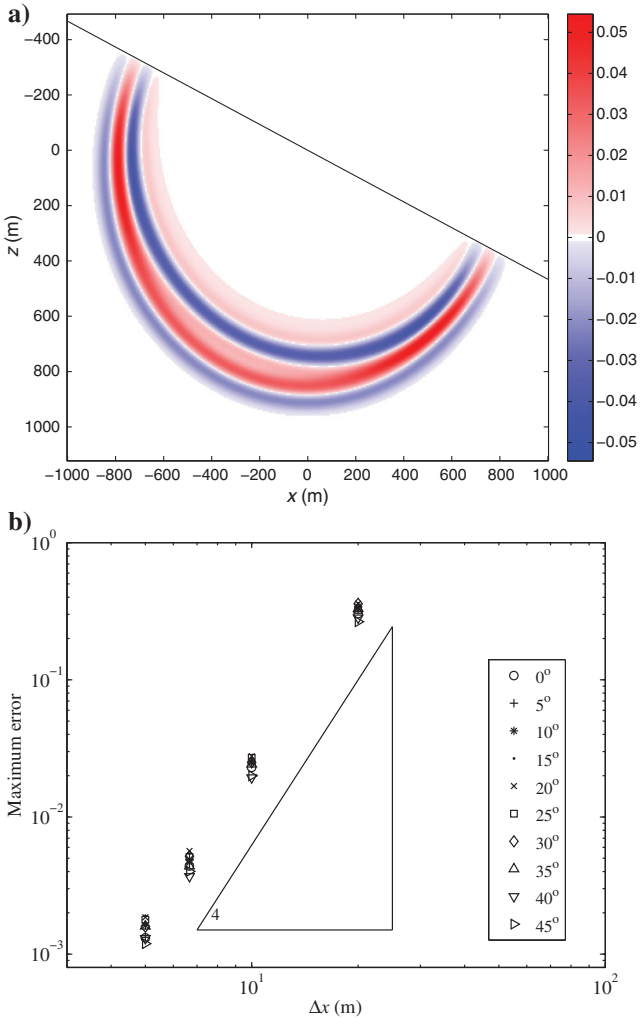

Figure 4. Pressure wavefield (a) after 0.4 s for a dip angle of 25° and (b) the maximum error at 0.4 s, relative to the maximum amplitude of in the solution, as a function of the grid spacing Δx for dip angles between 0° and 45°. The error behavior follows the fourth-order trend indicated by the slope of the large triangle.

2002). The wavelet has compact support and is a polynomial of the form

$$w(t) = -\left(\frac{T_w}{8}\right)^2 \frac{d^2}{dt^2}(1-\tau)^8 = (1-15\tau)(1-\tau)^6,$$
$$\text{for } \tau = (2t/T_w)^2 < 1, \tag{16}$$

and is zero otherwise. Here, the duration of the wavelet T_w is chosen such that its peak frequency f_{peak} is 15 Hz. Note that $(1/2)T_w f_{peak} = 0.934129$. Figure 4a displays the exact solution at a time of 0.4 s for a 25° dip. Figure 4b plots the maximum error at 0.4 s for a range of dip angles and grid spacings, Δx. The spacing in z obeys $\Delta z = \Delta x$ in this example. The observed numerical errors follow the fourth-order trend, despite the fact that the boundary condition is only an approximation for nonzero dip. The exact solution is antisymmetric in the direction normal to the free surface, whereas the discrete scheme assumes antisymmetry along the grid lines. The approximation apparently has little effect on the overall error in this first test problem, except for a small variation with dip angle.

The second 2D test problem has a smoothly varying velocity model

$$c(x,z) = c_0\{[1 - A\cos(x)\cosh(z)]^2 + [A\sin(x)\sinh(z)]^2\}^{-1/2}. \tag{17}$$

An exact solution on a grid that is periodic in $x \in [0, 2\pi)$ has a zero Neumann boundary condition at $z = 0$ and a zero Dirichlet boundary at the surface is

$$u(t,x,z) = \cos(mx_1 - \alpha t)\cos\left(\frac{1}{2}\pi z_1\right),\ \alpha = c_0\sqrt{m^2 + \left(\frac{1}{2}\pi\right)^2},$$
$$x_1 = x - A\sin(x)\cosh(z),\ z_1 = z - A\cos(x)\sinh(z) \in [-1, 0]. \tag{18}$$

The surface is implicitly defined by $z_1 = -1$. The time step was chosen at 10% of the stability limit, to reduce the size of the time-stepping error relative to the spatial discretization error. Figure 5a

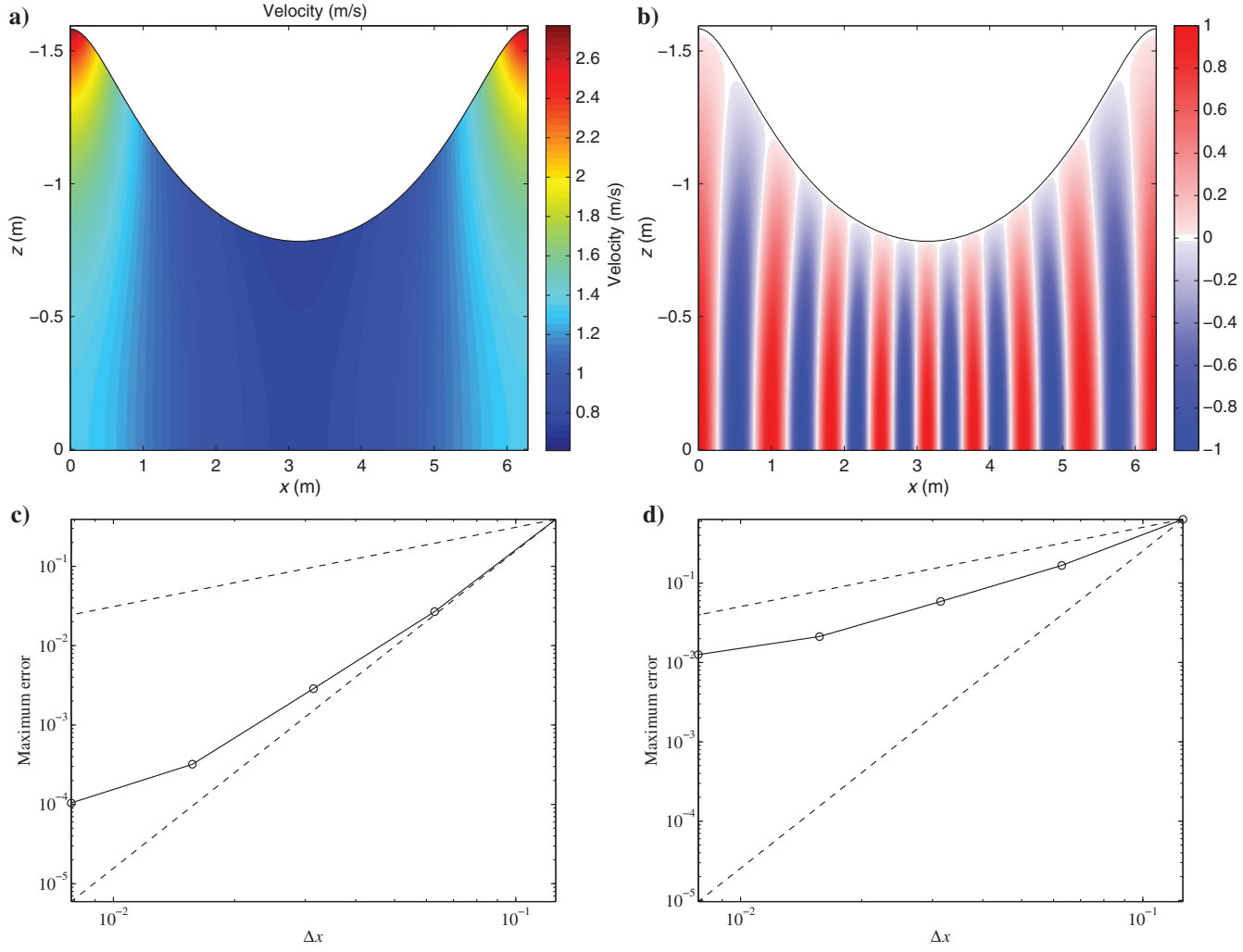

Figure 5. (a) Velocity model, (b) initial solution, and (c) errors on a log-log scale as a function of the grid spacing Δx as a drawn line. The dashed lines indicate the error behavior of a first- and a fourth-order scheme. The observed maximum errors for a trivial boundary scheme are included for reference (d).

shows the velocity model, and Figure 4b shows the solution at time 0 for $c_0 = 1$, $m = 8$, and $A = 1/4$. The maximum error at time $2\pi/c_0$ is shown in Figure 5c as a function of grid spacing Δx. The decrease of the observed error with grid spacing starts out like a fourth-order scheme for large spacings, but it deteriorates for smaller values of Δx, when the maximum error has dropped to 10^{-4}. For reference, Figure 5d displays the first-order error behavior for a trivial boundary scheme, in which solution values are set to zero above the free surface. Figure 5c shows that the simplified 1D scheme does not fully attain the fourth-order behavior of the interior finite-difference scheme, but the results are still a clear improvement over the trivial scheme of Figure 5d. The observed mean convergence rate of the maximum error for the latter is actually approximately 1.4, slightly better than the expected first-order trend.

The third test problem has a velocity model

$$c(x,z) = \frac{c_0\sqrt{2}}{L_0}[\cos(2xL_0) + \cosh(2zL_0)]^{-1/2}. \tag{19}$$

With a zero Dirichlet boundary conditions and zero source term, an exact standing-wave solution is

$$u(t,x,z) = \sin(\pi m_1 x_1/L_1)\sin(\pi m_2 z_1/L_1)\cos(\omega t),$$
$$\omega = \pi(c_0/L_1)\sqrt{m_1^2 + m_2^2}, \tag{20}$$

where

$$L_1 = \sin L_0, \quad x_1 = \sin(L_0 x)\cosh(L_0 z),$$
$$z_1 = \cos(L_0 x)\sinh(L_0 z), \quad x_1, z_1 \in [0, L_1]. \tag{21}$$

Figure 6 shows the velocity model when $c_0 = 1$, $L_1 = 0.8$, $m_1 = 7$, $m_2 = 5$, together with the initial solution and the resulting maximum error at time $T = 2\pi/\omega$ as a function of the grid spacing Δx on a log-log scale. It is evident from Figure 6c that the maximum error does not attain the fourth-order behavior of the interior scheme. It has a has a convergence rate closer to second order, worse than observed in the first experiment with the dipped flat surface. This

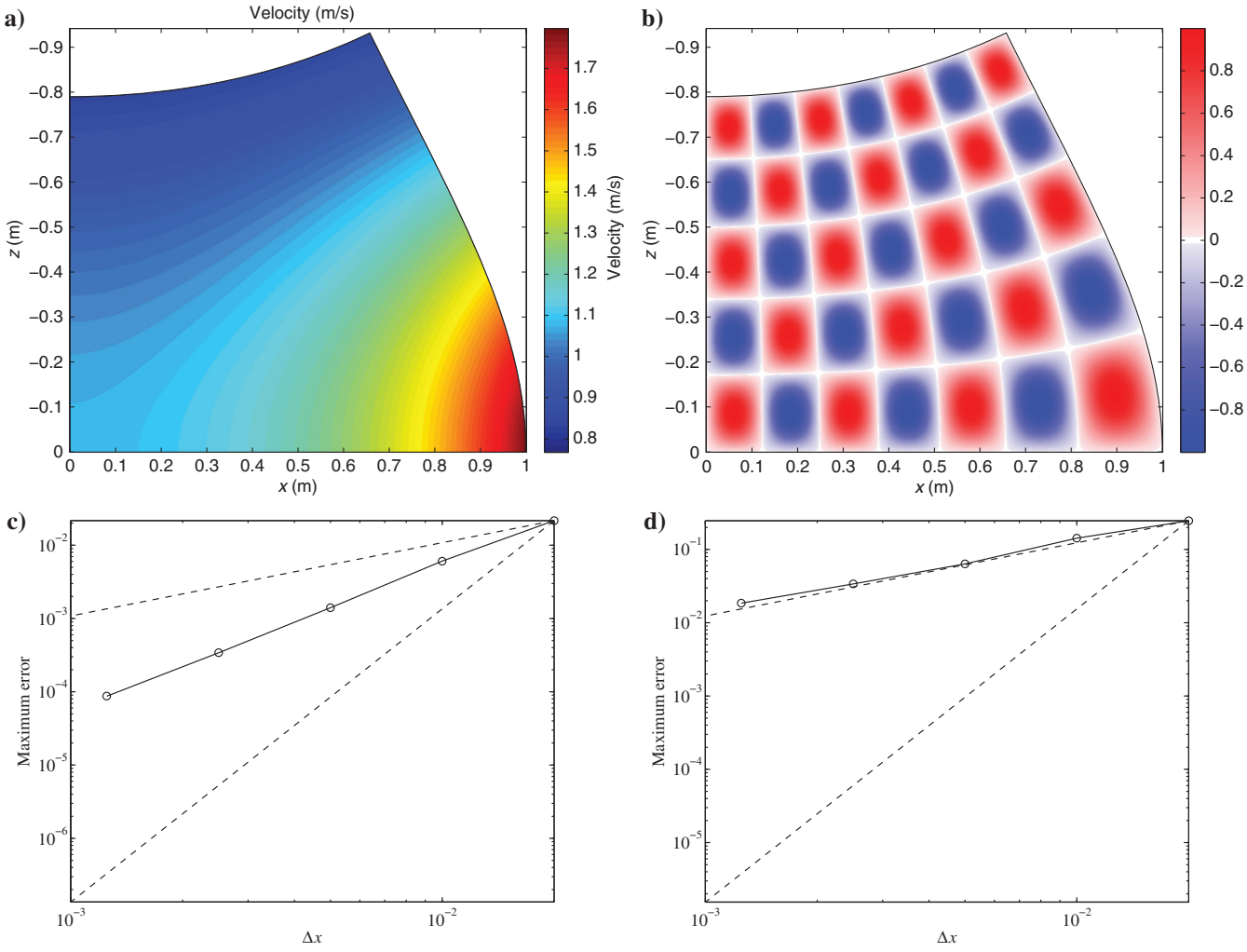

Figure 6. (a) Velocity model, (b) initial solution, and (c) errors on a log-log scale as a function of the grid spacing Δx as a drawn line, following a second-order trend. The dashed lines indicate error behavior that would have been observed with a first- or fourth-order schemes, respectively. The first-order error behavior observed for a trivial boundary scheme is included for reference (d).

is apparently the net effect of neglecting the boundary curvature and the spatial variability of the velocity model together with the application of the 1D boundary scheme along grid lines. For comparison, Figure 6d exhibits first-order convergence for the trivial scheme.

In practice, we can accept some loss of accuracy in a finite-difference code because a sharp internal contrast will have a similar effect. Across a discontinuity in the velocity model, the pressure will be continuous but not differentiable, leading to a local second-order spatial error. On top of that, if the velocity model is sampled point-wise, the position of the interface is only known with a first-order error.

The next problem is designed to test the method to its limits with a very rough topography created by a random number generator and some smoothing. The same holds for the geology underneath. Figure 7 displays the velocity model and a snapshot. The time step for this and the subsequent problems was set at half the maximum value dictated by the Courant–Friedrichs–Lewy (CFL) condition (Courant et al., 1928), to keep the time-stepping error sufficiently small. The grid spacing was 5 m. The source was placed at $x = 0$ m and a depth of −265 m, on a grid point well below the surface at −276.9 m, and the source signature was a 12 Hz Ricker wavelet. All boundaries are reflecting for testing purposes, with zero Dirichlet conditions at the free surface and zero Neumann conditions elsewhere.

The last two examples incorporate the actual topography of places on earth unlikely to see seismic data acquisition. Figure 8 depicts the topography of a line across the Vaalserberg, the highest point in The Netherlands, with the same velocity model as before, together with the computed seismogram. Again, the grid spacing is 5 m and the peak frequency of the Ricker wavelet 12 Hz. The shot was located at $x_s = 0$ m and a depth of −240 m, 12.9 m below the surface. Receivers at 5 m below the surface had lateral positions between $x_r = -987.5$ and +987.5 m, with a horizontal interval of 25 m.

Figure 9 displays the topography of a line across Half Dome with fantasized velocities underneath and a resulting seismogram. The source at $x_s = 0$ m and $z_s = -1230$ m was located 12.3 m below the surface. The wavelet and relative receiver positions were as before.

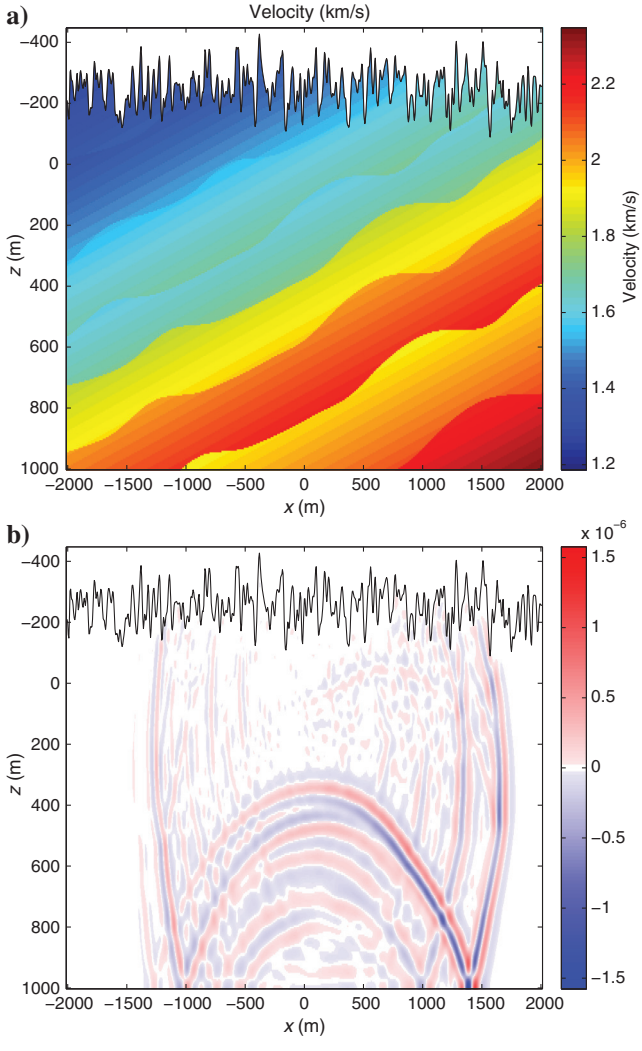

Figure 7. (a) Velocity model and (b) snapshot of the wavefield after 1 s for a source at the center, at a depth of 12 m below the surface. All boundaries are reflecting for testing purposes.

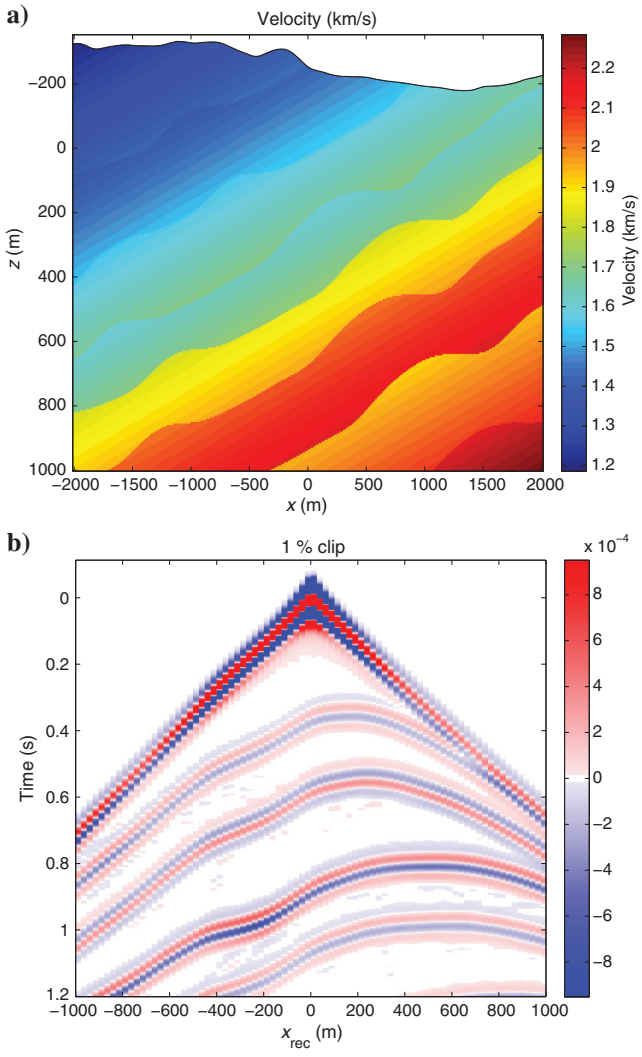

Figure 8. (a) Velocity model and (b) seismic data for a source at the center at a depth of 13 m below the surface.

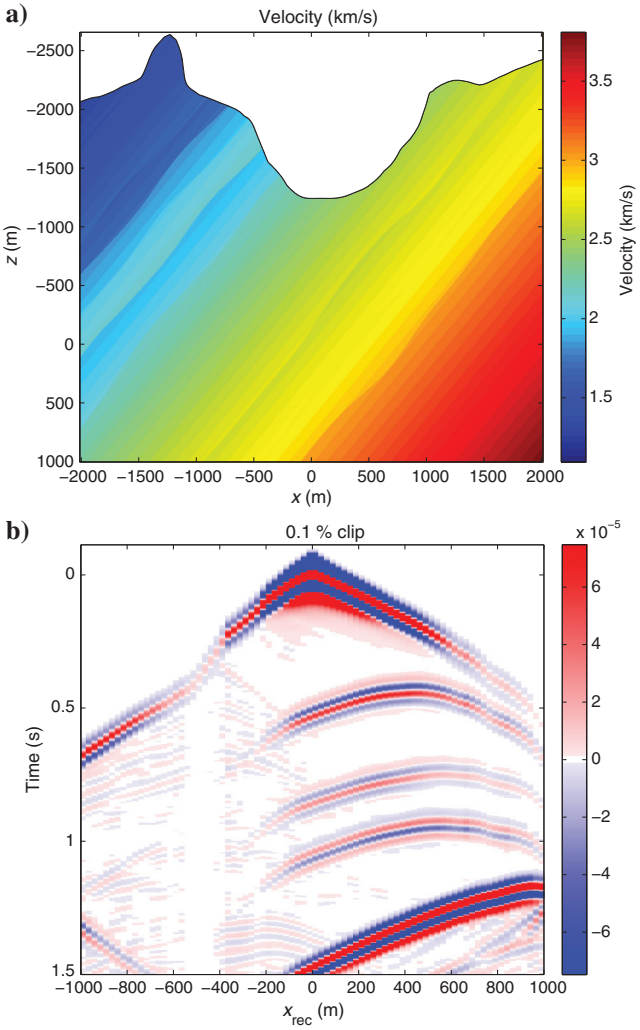

Figure 9. (a) Velocity model and (b) seismic data for a source at the center, at a depth of 12 m below the surface.

CONCLUSION

Modified finite-difference weights near the free surface enabled the incorporation of topography in a standard finite-difference scheme for the second-order constant-density acoustic wave equation. The method is a modification of an existing extrapolation scheme, simplified to a 1D operation with the additional constraint that the extrapolation excludes a point too close to the boundary, within half a grid spacing. This enables the method to run at the same stability limit as the interior scheme. For use in two dimensions, the approach was reformulated as a modified interior scheme by applying the standard finite-difference weights to the set of interior and extrapolated values per Cartesian coordinate direction. This avoids the ambiguities encountered in highly irregular topographies, where conflicting extrapolation results can be obtained from multiple directions. Although the implementation as a 1D operation per coordinate direction results in a simpler, stable, and more robust scheme, the price paid is some loss of accuracy. Because accuracy will also decrease near large contrasts in the interior model, this is likely to be acceptable in practice. The extension to three dimensions should be straightforward, although not entirely trivial, to implement.

APPENDIX A

STABILITY

The classic von Neumann stability analysis (Charney et al., 1950) leads to a time-step limit $\Delta t \le C_0 \Delta x / \max(c)$, with a CFL number

$$C_0 = 2\left(\sum_{k=1}^{M/2} \frac{4^k}{k^2 \binom{2k-1}{k-1}}\right)^{-1/2}, \tag{A-1}$$

for the centered second-derivative finite-difference operator of order M. This result holds for a constant sound speed c on an equidistant grid with periodic boundaries.

With the modified boundary and the resulting discrete second-derivative operator $\mathbf{D}_{xx}$, the 1D stability limit becomes

$$\Delta t \le \frac{2\Delta x}{\max(c)\sqrt{\| -\mathbf{D}_{xx}\|}}. \tag{A-2}$$

The symmetry of the spatial operator $\mathbf{D}_{xx}$ is lost with the boundary conditions considered here. However, numerical evaluation of the eigenvalues of $-\mathbf{D}_{xx}$ shows that they are real and nonnegative. The computation of the maximum eigenvalue for the example of Figure 2 over the range of $\xi \in (0, 1]$, which defines the position of the boundary in terms of the grid spacing Δx, provides Figure A-1, showing the ratio C/C_0 of the CFL number to its reference value in the periodic case. Here, C follows from the square root of the largest eigenvalue. Clearly, if one wants to run with the same CFL number as for the periodic case, scheme II is to be preferred.

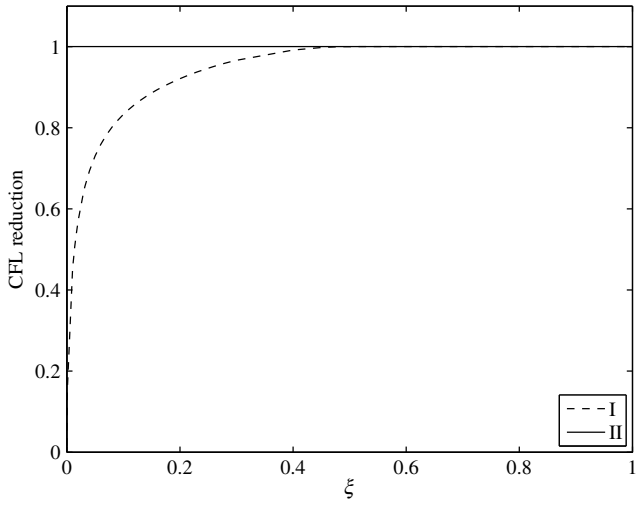

Figure A-1. Relative stability measured by C/C_0 for a spatial discretization of order $M = 8$ as a function of the position of the boundary, at $1 + \xi\Delta x$, for scheme I with $\xi_0 = 0$ or scheme II with $\xi_0 =$ ½, meaning that the extrapolation operator at the boundary excludes the interior point if its distance to the boundary is less than half a grid spacing.

REFERENCES

AlMuhaidib, A. M., M. Fehler, M. N. Toksöz, and Y. Zhang, 2011, Finite difference elastic wave modeling including surface topography: 81st Annual International Meeting, SEG, Expanded Abstracts, 2941–2946, doi: 10.1190/1.3627805.

Bartel, L. C., N. P. Symons, and D. F. Aldridge, 2000, Graded boundary simulation of air/earth interfaces in finite-difference elastic wave modeling: 70th Annual International Meeting, SEG, Expanded Abstracts, 2444–2447, doi: 10.1190/1.1815958.

Bohlen, T., and E. H. Saenger, 2006, Accuracy of heterogeneous staggered-grid finite-difference modeling of Rayleigh waves: Geophysics, **71**, no. 4, T109–T115, doi: 10.1190/1.2213051.

Boore, D. M., 1972, Finite difference methods for seismic wave propagation in heterogeneous materials, *in* B. A. Bolt, ed., Seismology: Surface waves and earth oscillations: Elsevier, 1–37.

Carpenter, M. H., J. Nordström, and D. Gottlieb, 1999, A stable and conservative interface treatment of arbitrary spatial accuracy: Journal of Computational Physics, **148**, 341–365, doi: 10.1006/jcph.1998.6114.

Charney, J. G., R. Fjörtoft, and J. von Neumann, 1950, Numerical integration of the barotropic vorticity equation: Tellus, **2**, 237–254, doi: 10.3402/tellusa.v2i4.8607.

Courant, R., K. Friedrichs, and H. Lewy, 1928, Über die partiellen Differenzengleichungen der mathematischen Physik: Mathematische Annalen, **100**, 32–74, doi: 10.1007/BF01448839.

Dablain, M. A., 1986, The application of high-order differencing to the scalar wave equation: Geophysics, **51**, 54–66, doi: 10.1190/1.1442040.

De la Puente, J., M. Ferrer, M. Hanzich, J. E. Castillo, and J. M. Cela, 2014, Mimetic seismic wave modeling including topography on deformed staggered grids: Geophysics, **79**, no. 3, T125–T141, doi: 10.1190/geo2013-0371.1.

Etienne, V, E. Chaljub, J. Virieux, and N. Glinsky, 2010, An hp-adaptive discontinuous Galerkin finite-element method for 3-D elastic wave modeling: Geophysical Journal International, **183**, 941–962, doi: 10.1111/j.1365-246X.2010.04764.x.

Fornberg, B., 1987, The pseudospectral method: Comparisons with finite-differences for the elastic wave equation: Geophysics, **52**, 483–501, doi: 10.1190/1.1442319.

Fornberg, B., 2010, A finite difference method for free boundary problems: Journal of Computational and Applied Mathematics, **233**, 2831–2840, doi: 10.1016/j.cam.2009.11.028.

Gao, L., R. Brossier, B. Pajot, J. Tago, and J. Virieux, 2015, An immersed free-surface boundary treatment for seismic wave simulation: Geophysics, **80**, no. 5, T193–T209, doi: 10.1190/geo2014-0609.1.

Hestholm, S., and B. Ruud, 1998, 3-D finite-difference elastic wave modeling including surface topography: Geophysics, **63**, 613–622, doi: 10.1190/1.1444360.

Hestholm, S., and B. Ruud, 2002, 3-D free-boundary conditions for coordinate-transform finite-difference seismic modeling: Geophysical Prospecting, **50**, 463–474, doi: 10.1046/j.1365-2478.2002.00327.x.

Hicks, G. J., 2002, Arbitrary source and receiver positioning in finite-difference schemes using Kaiser windowed sinc function: Geophysics, **67**, 156–165, doi: 10.1190/1.1451454.

Hu, W., 2016, An improved immersed boundary finite-difference method for seismic wave propagation modeling with arbitrary surface topography: Geophysics, **81**, no. 6, T311–T322, doi: 10.1190/geo2016-0094.1.

Komatitsch, D., and J.-P. Vilotte, 1998, The spectral element method: An efficient tool to simulate the seismic response of 2-D and 3-D geological structures: Bulletin of the Seismological Society America, **88**, 368–392.

Lax, P., and B. Wendroff, 1960, Systems of conservation laws: Communications on Pure and Applied Mathematics, **13**, 217–237, doi: 10.1002/cpa.3160130205.

Lipnikov, K., G. Manzini, and M. Shashkov, 2014, Mimetic finite difference method: Journal of Computational Physics, **257**, 1163–1227, doi: 10.1016/j.jcp.2013.07.031.

Lombard, B., J. Piraux, C. Gélis, and J. Virieux, 2008, Free and smooth boundaries in 2-D finite-difference schemes for transient elastic waves: Geophysical Journal International, **172**, 252–261, doi: 10.1111/j.1365-246X.2007.03620.x.

Mattsson, K., F. Ham, and G. Iaccarino, 2009, Stable boundary treatment for the wave equation on second-order form: Journal of Scientific Computing, **41**, 366–383, doi: 10.1007/s10915-009-9305-1.

Mattsson, K., and J. Nordström, 2006, High order finite difference methods for wave propagation in discontinuous media: Journal of Computational Physics, **220**, 249–269, doi: 10.1016/j.jcp.2006.05.007.

Mittet, R., 2002, Free-surface boundary conditions for elastic staggered-grid modeling schemes: Geophysics, **67**, 1616–1623, doi: 10.1190/1.1512752.

Piraux, J., and B. Lombard, 2001, A new interface method for hyperbolic problems with discontinuous coefficients: One-dimensional acoustic example: Journal of Computational Physics, **168**, 227–248, doi: 10.1006/jcph.2001.6696.

Robertsson, J. O., 1996, A numerical free-surface condition for elastic/viscoelastic finite-difference modeling in the presence of topography: Geophysics, **61**, 1921–1934, doi: 10.1190/1.1444107.

Seo, J. H., and R. Mittal, 2011, A high-order immersed boundary method for acoustic wave scattering and low-mach number flow-induced sound in complex geometries: Journal of Computational Physics, **230**, 1000–1019, doi: 10.1016/j.jcp.2010.10.017.

Shortley, G. H., and R. Weller, 1938, Numerical solution of Laplace's equation: Journal of Applied Physics, **9**, 334–348, doi: 10.1063/1.1710426.

Shubin, G. R., and J. B. Bell, 1987, A modified equation approach to constructing fourth order methods for acoustic wave propagation: SIAM Journal on Scientific and Statistical Computing, **8**, 135–151, doi: 10.1137/0908026.

Strand, B., 1994, Summation by parts for finite difference approximations for d/dx: Journal of Computational Physics, **110**, 47–67, doi: 10.1006/jcph.1994.1005.

Tessmer, E., and D. Kosloff, 1994, 3-D elastic modeling with surface topography by a Chebychev spectral method: Geophysics, **59**, 464–473, doi: 10.1190/1.1443608.

Zeng, C., J. Xia, R. D. Miller, and G. P. Tsoflias, 2012, An improved vacuum formulation for 2-D finite-difference modeling of Rayleigh waves including surface topography and internal discontinuities: Geophysics, **77**, no. 1, T1–T9, doi: 10.1190/geo2011-0067.1.

Zhang, D., G. Schuster, and G. Zhan, 2013, Multi-source least-squares reverse time migration with topography: 83rd Annual International Meeting, SEG, Expanded Abstracts, 3736–3740, doi: 10.1190/segam2013-0270.1.

Zhebel, E., S. Minisini, A. Kononov, and W. A. Mulder, 2011, Solving the 3-D acoustic wave equation with higher-order mass-lumped tetrahedral finite elements: 73rd Annual International Conference and Exhibition, EAGE, Extended Abstracts, A010, doi: 10.3997/2214-4609.20148952.

Zhebel, E., S. Minisini, A. Kononov, and W. A. Mulder, 2014, A comparison of continuous mass-lumped finite elements with finite differences for 3-D wave propagation: Geophysical Prospecting, **62**, 1111–1125, doi: 10.1111/1365-2478.12138.